



SPWID 2023

The Ninth International Conference on Smart Portable, Wearable, Implantable
and Disability-oriented Devices and Systems

ISBN: 978-1-68558-075-9

June 26 - 30, 2023

Nice, France

SPWID 2023 Editors

Lorena Parra Boronat, Universitat Politecnica de Valencia, Spain

SPWID 2023

Forward

The Ninth International Conference on Smart Portable, Wearable, Implantable and Disability-oriented Devices and Systems (SPWID 2023), held between June 26th and June 30th, 2023, continued a series of events bridging the concepts and the communities dealing with specialized implantable, wearable, near-body, or mobile devices, including artificial organs, body-driven technologies, and assistive services. Mobile communications played by the proliferation of smartphones and practical aspects of designing such systems and developing specific applications raise challenges for successful acceptance and deployment.

We take here the opportunity to warmly thank all the members of the SPWID 2023 technical program committee, as well as all the reviewers. The creation of such a high-quality conference program would not have been possible without their involvement. We also kindly thank all the authors who dedicated much of their time and effort to contribute to SPWID 2023. We truly believe that, thanks to all these efforts, the final conference program consisted of top-quality contributions. We also thank the members of the SPWID 2023 organizing committee for their help in handling the logistics of this event.

We hope that SPWID 2023 was a successful international forum for the exchange of ideas and results between academia and industry and for the promotion of progress in the field of smart portable, wearable, implantable and disability-oriented devices, and systems.

SPWID 2023 Chairs

SPWID 2023 Steering Committee

Steve Mann, Stanford University, USA

Mu-Chun Su, National Central University, Taiwan

Andrea Caroppo, National Research Council of Italy (CNR) - Institute for Microelectronics and Microsystems, Italy

SPWID 2023 Publicity Chairs

Sandra Viciano Tudela, Universitat Politècnica de València, Spain

José Miguel Jiménez, Universitat Politècnica de València, Spain

SPWID 2023 Committee

SPWID 2023 Steering Committee

Steve Mann, Stanford University, USA
Mu-Chun Su, National Central University, Taiwan
Andrea Caroppo, National Research Council of Italy (CNR) - Institute for Microelectronics and Microsystems, Italy

SPWID 2023 Publicity Chairs

Sandra Viciano Tudela, Universitat Politècnica de Valencia, Spain
José Miguel Jiménez, Universitat Politècnica de Valencia, Spain

SPWID 2023 Technical Program Committee

Zaid Ahmad, COMSATS University Islamabad, Pakistan
Giovanni Albani, Istituto Auxologico Italiano - IRCCS, Italy
Jesús B. Alonso Hernández, Institute for Technological Development and Innovation in Communications (IDeTIC) | University of Las Palmas de Gran Canaria (ULPGC), Spain
Salzitsa Anastasova-Ivanova, Imperial College London, UK
Danilo Avola, Sapienza University, Rome, Italy
Suhaib Ahmed Batt, Baba Ghulam Shah Badshah University, India
Roberto Beghi, Università degli Studi di Milano, Italy
Juan-Vicente Capella-Hernández, Universitat Politècnica de València, Spain
Andrea Caroppo, National Research Council of Italy (CNR) - Institute for Microelectronics and Microsystems, Italy
Claude Chaudet, Webster University Geneva, Switzerland
Francesco G. Della Corte, University of Napoli Federico II, Italy
Abdelali Elmoufidi, University of Hassan II Casablanca, Morocco
Biyi Fang, Microsoft, USA
Shayan Fazeli, UCLA Henry Samueli School of Engineering and Applied Science, USA
Giancarlo Fortino, University of Calabria, Italy
Arfan Ghani, Coventry University, UK
Migyeong Gwak, University of California - Los Angeles (UCLA), USA
Gema Ibáñez, ITACA - Universitat Politècnica de València, Spain
Jk Jensen, Arizona State University, USA
Pradeep Kumar, University of KwaZulu-Natal, Durban, South Africa
Tomas Lorenzo, University of Colorado at Boulder, USA
Alessandro Leone, National Research Council of Italy, Lecce, Italy
Lenka Lhotska, Czech Institute of Informatics, Robotics and Cybernetics | Czech Technical University in Prague, Czech Republic
Cun Li, Eindhoven University of Technology, Netherlands
Tianliang Li, Wuhan University of Technology, China
Steve Mann, Stanford University, USA
Tauheed Khan Mohd, Augustana College, USA

Gregory O'Hare, University College Dublin (UCD), Ireland
Ilham El Ouariachi, University Sidi Mohamed Ben Abdellah, Fez, Morocco
Luana Persano, Institute of Nanoscience - CNR, Pisa, Italy
Chinthaka Premachandra, Shibaura Institute of Technology, Japan
Amir Rahmati, Stony Brook University, USA
Veronica Mattioli, Univeristy of Parma, Italy
Helder C. R. Oliveira, University of Calgary, Canada
Juha Röning, University of Oulu, Finland
Gonzalo Sad, CIFASIS / CONICET / FCEIA | Universidad Nacional de Rosario, Argentina
Mu-Chun Su, National Central University, Taiwan
Ryszard Tadeusiewicz, AGH University of Science and Technology, Poland
Adrian Tarniceriu, Securecell SA, Switzerland
Carlos M. Travieso-González, University of Las Palmas de Gran Canaria, Spain
Warner ten Kate, Philips Research, Eindhoven, Netherlands
Wang Wen, Institute of Acoustics - Chinese Academy of Sciences, China
Diane Woodbridge, University of San Francisco, USA
Murat Kaya Yapici, Sabanci University, Istanbul, Turkey

Copyright Information

For your reference, this is the text governing the copyright release for material published by IARIA.

The copyright release is a transfer of publication rights, which allows IARIA and its partners to drive the dissemination of the published material. This allows IARIA to give articles increased visibility via distribution, inclusion in libraries, and arrangements for submission to indexes.

I, the undersigned, declare that the article is original, and that I represent the authors of this article in the copyright release matters. If this work has been done as work-for-hire, I have obtained all necessary clearances to execute a copyright release. I hereby irrevocably transfer exclusive copyright for this material to IARIA. I give IARIA permission to reproduce the work in any media format such as, but not limited to, print, digital, or electronic. I give IARIA permission to distribute the materials without restriction to any institutions or individuals. I give IARIA permission to submit the work for inclusion in article repositories as IARIA sees fit.

I, the undersigned, declare that to the best of my knowledge, the article does not contain libelous or otherwise unlawful contents or invading the right of privacy or infringing on a proprietary right.

Following the copyright release, any circulated version of the article must bear the copyright notice and any header and footer information that IARIA applies to the published article.

IARIA grants royalty-free permission to the authors to disseminate the work, under the above provisions, for any academic, commercial, or industrial use. IARIA grants royalty-free permission to any individuals or institutions to make the article available electronically, online, or in print.

IARIA acknowledges that rights to any algorithm, process, procedure, apparatus, or articles of manufacture remain with the authors and their employers.

I, the undersigned, understand that IARIA will not be liable, in contract, tort (including, without limitation, negligence), pre-contract or other representations (other than fraudulent misrepresentations) or otherwise in connection with the publication of my work.

Exception to the above is made for work-for-hire performed while employed by the government. In that case, copyright to the material remains with the said government. The rightful owners (authors and government entity) grant unlimited and unrestricted permission to IARIA, IARIA's contractors, and IARIA's partners to further distribute the work.

Table of Contents

A Prototype towards a Test Bench for Noninvasive Transcutaneous Carbon Dioxide Monitoring Devices <i>Zakaria Tichout, Pierre Grangeat, Veronique Mourier, Rodrigue Rousier, and Stephane Colin</i>	1
Skin Lesion Segmentation and Classification Using Deep Learning Methods <i>Spyridon Vallas, Isidoros Perikos, and Michael Paraskevas</i>	5

A Prototype towards a Test Bench for Noninvasive Transcutaneous Carbon Dioxide Monitoring Devices

Tichout Zakaria
Micro-technologies for Biology and
Healthcare
Univ. Grenoble Alpes, CEA, LETI,
MINATEC Campus
Grenoble, France
e-mail: zakaria.tichout@cea.fr

Pierre Grangeat
Micro-technologies for Biology and
Healthcare
Univ. Grenoble Alpes, CEA, LETI,
MINATEC Campus
Grenoble, France
e-mail: pierre.grangeat@wanadoo.fr

Véronique Mourier
Micro-technologies for Biology and
Healthcare
Univ. Grenoble Alpes, CEA, LETI,
MINATEC Campus
Grenoble, France
e-mail: veronique.mourier@cea.fr

Rodrigue Rousier †
Micro-technologies for Biology and Healthcare
Univ. Grenoble Alpes, CEA, LETI, MINATEC Campus
Grenoble, France
e-mail: rodrigue.rousier@cea.fr

Stéphane Colin
Institut Clément Ader
Univ. de Toulouse, CNRS-INSA-ISAE-Mines Albi-UPS
Toulouse, France
e-mail: colin@insa-toulouse.fr

† Corresponding author.

Abstract— Dioxygen and carbon dioxide arterial partial pressures are important clinical parameters that enable to assess the respiratory status of a patient. That is why they are continuously monitored in intensive care units, where large and expensive bedside devices are used. To grant access to continuous monitoring of these parameters to a larger portion of patients, smaller and noninvasive medical devices were developed to measure transcutaneous dioxygen and carbon dioxide concentrations. They accurately estimate the partial pressures of those gases based on measurements made at the level of the skin. These devices are validated through clinical trials, which require long and expensive procedures. Developing advanced test benches mimicking human physiology is an interesting alternative to mature medical devices before submitting them to clinical trials. This work presents, to the best of our knowledge, a first-of-its-kind test bench prototype that mimics blood and skin for testing transcutaneous carbon dioxide monitoring medical devices. We also propose a proof-of-concept method to monitor dissolved carbon dioxide using common chemistry laboratory sensors. A similar test bench for transcutaneous dioxygen is currently under development.

Keywords- test bench; transcutaneous gas monitoring; carbon dioxide partial pressure.

I. INTRODUCTION

Blood gas analysis enables to detect and interpret respiratory, circulatory and metabolic disorders [1]. It is a common diagnostic tool for critically ill patients in intensive care departments. The reference method to analyze blood gases requires arterial sampling, an invasive and painful method. As an alternative, medical devices for transcutaneous gas monitoring were conceived in a noninvasive approach [2][3]. Developing and validating such devices require clinical trials, at the cost of a long and expensive procedure. An interesting option is to develop these devices using test benches that mimic human

physiology up to a certain level of maturity before validating them in clinical trials [3].

Such test benches would require generating a gaseous partial pressure starting from a liquid phase. Therefore, monitoring the concentration in the aqueous phase is necessary for an accurate test bench. The blood gases of interest are dioxygen O_2 and carbon dioxide CO_2 and this work focuses on the latter. The classical principle exploited by reference sensors for measuring dissolved CO_2 concentration is diffusion through a selective hydrophobic membrane to get CO_2 molecules in a gaseous phase inside the sensor. The gas concentration is then measured using an optical method, typically based on infrared absorption. Such sensors suffer from a slow response due to the diffusion phenomenon in the sensor chamber, leading to a slow response time: a 10 min $Tr_{99\%}$ response in the case of AquaMS sensor [4], the cost of which is around 10 k€. PreSens [5] offers a quicker sensor, delivering results in a few seconds, with a principle based on optical quenching using selective photosensible spots directly in the solution, getting rid of the diffusion part, but for a higher price around 15k€.

The work described in Section II aims to offer an alternative to these sensors by measuring dissolved carbon dioxide indirectly, using common chemistry laboratory devices. Section III presents a test bench prototype that mimics transcutaneous carbon dioxide at the level of the forearm. We conclude our work in Section IV.

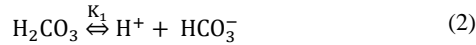
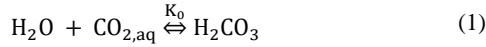
II. A METHOD TO MEASURE DISSOLVED CARBON DIOXIDE IN A CONTROLLED ENVIRONMENT

The controlled environment of interest is the liquid phase that is used to simulate blood in the test bench (see Section III). A physiological solution is a possible option. In this study, an aqueous solution of sodium chloride NaCl at 0.9% is used. It allows to monitor the pH and salinity of the liquid phase without any chemical reaction between chloride or sodium ions and the carbon dioxide CO_2 or the ions resulting

from its dissolution in water. Therefore, the dissolution of CO_2 in an aqueous solution of NaCl follows the same steps as in water.

A. Theory

Carbon dioxide CO_2 , after dissolution in water, leads to the formation of carbonic acid H_2CO_3 , a weak acid that dissociates into bicarbonate ions HCO_3^- then to carbonate ions CO_3^{2-} in cascade reactions [4][5] :



Reaction 1 represents the CO_2 hydration equation, and has a low equilibrium constant $K_0 \approx 10^{-7}$ [6], which means that $\text{CO}_{2,\text{aq}}$ concentration exceeds greatly H_2CO_3 concentration. The concentration of all dissolved CO_2 will be referred to as the concentration of $\text{CO}_{2,\text{aq}}$ and the thermodynamic equilibrium between a gaseous phase and the aqueous phase is described by Henry's law:

$$[\text{CO}_{2,\text{aq}}] = \alpha P_{\text{CO}_2} \quad (4)$$

where $[\text{CO}_{2,\text{aq}}]$ (mol L^{-1}) is the concentration in the aqueous phase, P_{CO_2} (Pa) is the partial pressure in the gaseous phase and $\alpha = K_0 K_{\text{CO}_{2,0}}$ with $K_{\text{CO}_{2,0}}$ the molar solubility of carbon dioxide in the aqueous solution, which depends on pressure, temperature, salinity, ionic strength and dissolved organic matter [4][6]. This study is conducted at ambient pressure, and the variables are the temperature T (K) and salinity S (ppt). Therefore, the solubility is computed as follows [6]:

$$\ln(K_{\text{CO}_{2,0}}) = -58.09 + 90.05 \left(\frac{T_0}{T}\right) + 22.29 \ln\left(\frac{T}{T_0}\right) + S \left[-0.68 + 0.40 \left(\frac{T}{T_0}\right) - 0.06 \left(\frac{T}{T_0}\right)^2 \right] \quad (5)$$

with $T_0 = 100$ K. The equilibrium constants K_1 and K_2 of reactions 2 and 3 are defined as follows:

$$K_1 = \frac{[\text{H}^+][\text{HCO}_3^-]}{[\text{H}_2\text{CO}_3] C_0} \quad (6)$$

$$K_2 = \frac{[\text{H}^+][\text{CO}_3^{2-}]}{[\text{HCO}_3^-] C_0} \quad (7)$$

where $[X]$ represents the molar concentration of species X , and $C_0 = 1 \text{ mol L}^{-1}$.

The electrical conductivity of the solution is a necessary parameter for the computation. The Kohlrausch law applied to the studied system results in the following equation:

$$\sigma = \lambda_{\text{HCO}_3^-} [\text{HCO}_3^-] + 2\lambda_{\text{CO}_3^{2-}} [\text{CO}_3^{2-}] + \lambda_{\text{H}^+} [\text{H}^+] + \lambda_{\text{OH}^-} [\text{OH}^-] + \lambda_{\text{Na}^+} [\text{Na}^+] + \lambda_{\text{Cl}^-} [\text{Cl}^-] \quad (8)$$

where σ (S m^{-1}) is the electrical conductivity of the solution and λ_X ($\text{S m}^{-1} \text{ mol}^{-1} \text{ L}$) is the molar conductivity of ion X .

The ionic product of water K_w is defined as follows [9]:

$$K_w = \frac{[\text{H}^+][\text{OH}^-]}{C_0^2} \quad (9)$$

B. Method proposed to measure dissolved carbon dioxide

The concentration of CO_2 can be computed by combining (6), (7), (8) and (9):

$$[\text{CO}_{2,\text{aq}}] = \frac{\sigma - \lambda_{\text{H}^+} [\text{H}^+] - \lambda_{\text{OH}^-} \frac{K_w}{[\text{H}^+]} - \lambda_{\text{Na}^+} [\text{Na}^+] - \lambda_{\text{Cl}^-} [\text{Cl}^-]}{\frac{\lambda_{\text{HCO}_3^-} K_1}{[\text{H}^+]} + \frac{2\lambda_{\text{CO}_3^{2-}} K_1 K_2}{[\text{H}^+]^2}} \quad (10)$$

Equation (10) shows that measuring the pH and the conductivity allows to compute the concentration of dissolved CO_2 in an aqueous solution of known NaCl concentration. The measurement of temperature is also necessary, as the constants used in (10) are temperature-dependent thermodynamic parameters. The evolution of the equilibrium constants with respect to the temperature is the following:

$$\text{p}K_1 = \frac{T_1}{T} + \frac{T}{T_2} - 14.84 \quad (11)$$

where $K_1 = 10^{-\text{p}K_1}$, $T_1 = 3404.71$ K and $T_2 = 30.49$ K [10].

$$\text{p}K_2 = \frac{T_3}{T} + \frac{T}{T_4} - 6.49 \quad (12)$$

where $K_2 = 10^{-\text{p}K_2}$, $T_3 = 2902.39$ K and $T_4 = 42.03$ K [11].

$$\ln(K_w) = 148.98 - \frac{T_5}{T} - 23.6521 \ln\left(100 \frac{T}{T_0}\right) \quad (13)$$

where $T_5 = 13847.26$ K and $T_0 = 100$ K [9].

The evolution of the molar conductivity λ_X of the ions of interest with respect to the temperature was not found in the literature. Hence, it was extracted from the Nernst-Einstein equation [12]:

$$\lambda_X = \frac{D_X Z_X F^2}{RT} \quad (14)$$

where D_X ($\text{m}^2 \text{ s}^{-1}$) is the binary diffusion coefficient of ion X in water and Z_X its charge, F (C mol^{-1}) the Faraday constant, R ($\text{J mol}^{-1} \text{ K}^{-1}$) the ideal gas constant, T (K) the temperature.

To compute the molar conductivity at different temperatures, a Taylor expansion to the first order is applied to (14) around $T_6 = 298.15$ K, the temperature at which the values of molar conductivity are given in the literature. D_X is also a temperature-dependent thermodynamic parameter. However, it will be considered constant and its value is taken at $T = T_6$:

$$\lambda_X(T) = \lambda_X(T_6) + \frac{D_X Z_X F^2}{R} \times \left(\frac{1}{T} - \frac{1}{T_6}\right) \quad (15)$$

In conclusion, we show that injecting the measurements of pH, conductivity and temperature in (10) and (15) allows to compute the concentration of dissolved carbon dioxide.

III. TEST BENCH CONCEPTION

The test bench aims to generate carbon dioxide to test a noninvasive transcutaneous CO_2 gas sensor that is yet to be developed. The bench has the specifications of the measurement site, which is the forearm. The end goal is to generate the same carbon dioxide partial pressure P_{CO_2} and flux Φ_{CO_2} . A liquid phase is used to simulate the blood and a membrane to simulate the skin, as shown in Figure 1. A liquid phase was chosen instead of a gaseous phase to mimic the kinetics of diffusion in the aqueous phase and through the membrane. Transcutaneous gas measurement devices can heat the skin up to 42°C , hence the test bench parameters are determined at both 37 and 42°C .

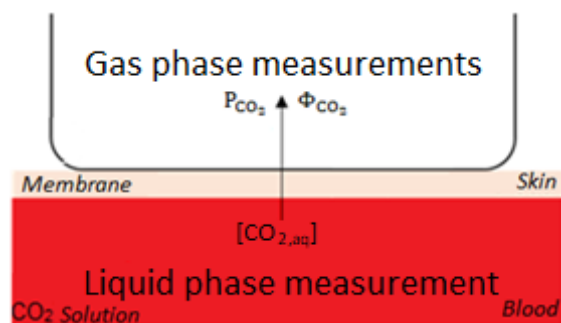


Figure 1. Test bench schematic diagram

A. Test bench conception

P_{CO_2} varies between 2.66 and 13.33 kPa (20 and 100 mmHg) [13]. At 42°C , using (4) and (5), the corresponding $[\text{CO}_{2,\text{aq}}]$ ranges from 0.6 to 3 mmol L^{-1} . In order to mimic the kinetics of carbon dioxide diffusion in blood, the bench has to generate a CO_2 flux of $7.54 \cdot 10^{-7}$ $\text{mol m}^{-2} \text{s}^{-1}$ as it is the case at the level of the forearm [14]. To be able to do so, simulations at our lab show that the depth of the liquid in the tank (see Figure 2 right) has to be 3 and 12 mm for a 37 and 42°C temperature, respectively.

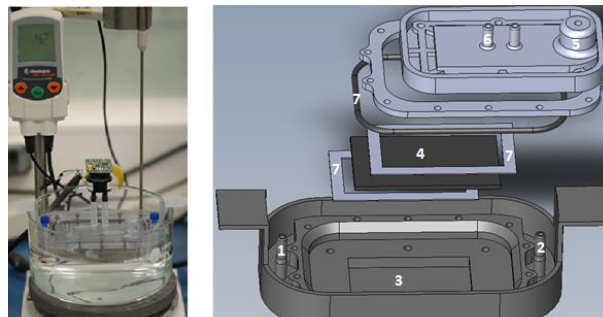
The skin is represented by a polymer membrane that exhibits similar carbon dioxide diffusion properties as human skin at the level of the forearm. The selection was made on the basis of the permeability, defined by Krogh's diffusion constant:

$$K_r = \frac{k \cdot x}{P_{\text{air}}} \quad (16)$$

where K_r is the Krogh coefficient ($\text{m}^2 \text{s}^{-1} \text{Pa}^{-1}$), k the mass transfer coefficient (m s^{-1}), x the thickness (m) of the membrane and P_{air} the total air pressure (Pa) at the membrane temperature. A polydimethylsiloxane membrane (PDMS) of thickness 4.3 and 2.8 mm can mimic the skin [15] at 37 and 42°C , respectively.

B. Experimental setup and results

To create a liquid phase with the mentioned concentrations, CO_2 stock solutions Standard Hanna HI



1: inlet, 2: outlet, 3: tank, 4: membrane, 5: vent, 6: CO_2 sensor connection, 7: seals

Figure 2. Left: test bench. Right: architecture of the test bench

$4005\text{-}01$ at 0.1 mol L^{-1} and Reagecon SC026C at 6 g L^{-1} were diluted in an Otec sodium chloride 0.9% sterile pyrogen-free solution.

The test bench is a closed chamber designed using SolidWorks (Figure 2 right) and crafted in non-permeable materials to carbon dioxide. It includes a circulatory system composed of the inlet, the tank and the outlet in order to mimic blood circulation. On top of the liquid phase, sits the membrane that represents the skin and finally the connection with the carbon dioxide sensor. The test bench is maintained at 42°C using a bain-marie, heated by a temperature-regulated stirrer. The carbon dioxide generated by the test bench was measured using a SprintIR-WP20 gas sensor (Figure 2 left).

Equation (10) requires the measurement of the pH, the conductivity and the temperature of the solution in order to compute its concentration in carbon dioxide. In this work, bench-top measuring instrument Orion™ Versa Star Pro™ VSTAR 52 was used. Using an extra conductivity module, this device allows to measure the salinity also. These measurements were made inside the glass reactor that supplies the bench test tank through a peristaltic pump.

The $[\text{CO}_{2,\text{aq}}]$ range has been explored through five measurement points: starting from a solution of 3 mmol L^{-1} and diluting up to 0.6 mmol L^{-1} . The intermediary concentrations at which measurements were made are 1.2 , 1.8 and 2.4 mmol L^{-1} , they are referred to as measurement points. At each point, conductivity, pH and temperature were measured to compute $\text{CO}_{2,\text{aq}}$ concentration using (10). Each measurement was repeated five times to create five-fold measurement points and assess the stability and reproducibility of the experiment. Five minutes separated each dilution to allow the solution to reach equilibrium.

Equation (10) shows a linear relationship between $[\text{CO}_{2,\text{aq}}]$ and conductivity, and between $[\text{CO}_{2,\text{aq}}]$ logarithm and pH. Therefore, three values of each five-fold measurement point were randomly chosen to create a linear regression learning batch. The resulting linear regression ‘‘Predicted value’’ was

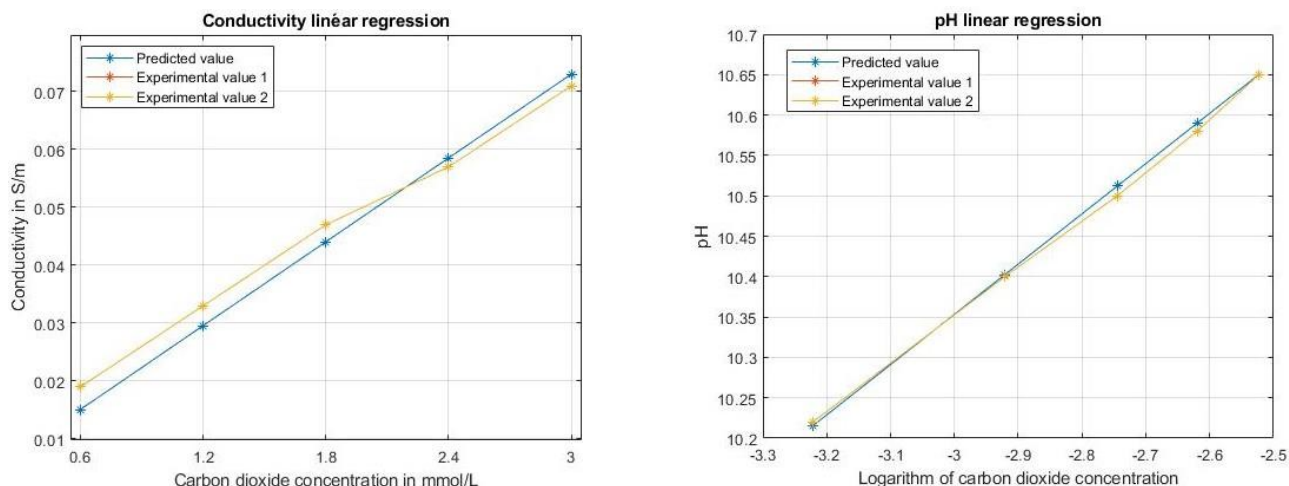


Figure 3. Left: Conductivity linear regression. Right: pH linear regression

plotted against the experimental values “Experimental value 1” and “Experimental value 2”.

Figure 3 shows that the experimental results validate the proposed method based on (10). It also proves the reproducibility of the experiments and the stability of the measurements.

IV. DISCUSSION AND CONCLUSION

The results obtained so far from of this ongoing work show that it is possible to compute $[CO_{2,aq}]$ from the measurement of pH and conductivity. This indirect measurement is also valid for the dynamic regime and not only at equilibrium as Figure 3 was obtained by consecutive dilutions. The devices used in this approach have a few seconds time response, allowing real-time monitoring of $[CO_{2,aq}]$ using the method proposed in Section II.B. The aim is to be able to control the partial pressure in the gaseous phase above the membrane by adjusting the concentration in the aqueous phase. A previous study worked on developing a model describing the relationship between these two physical quantities [16].

ACKNOWLEDGMENT

This work was partially supported by L3Medical, a CEA partner. We also express our gratitude to our colleagues of the Micro-technologies for Biology and Healthcare department of CEA Grenoble for their expertise conducting this project.

REFERENCES

- [1] L. Gattinoni, A. Pesenti, and M. Matthay, “Understanding blood gas analysis,” *Intensive Care Med*, vol. 44, no. 1, pp. 91–93, Jan. 2018, doi: 10.1007/s00134-017-4824-y.
- [2] I. Costanzo, D. Sen, L. Rhein, and U. Guler, “Respiratory Monitoring: Current State of the Art and Future Roads,” *IEEE Rev. Biomed. Eng.*, vol. 15, pp. 103–121, 2022, doi: 10.1109/RBME.2020.3036330.
- [3] P. Grangeat *et al.*, “Evaluation in Healthy Subjects of a Transcutaneous Carbon Dioxide Monitoring Wristband during Hypo and Hypercapnia Conditions,” in *2020 42nd Annual International Conference of the IEEE Engineering in Medicine & Biology Society (EMBC)*, Montreal, QC, Canada: IEEE, Jul. 2020, pp. 4640–4643. doi: 10.1109/EMBC44109.2020.9175876.
- [4] “Aquams - Sonde CO2 dissous,” *aquams*. <https://www.aquams.com/mesure-en-continu/sonde-co2-dissous/> (accessed Jun. 19, 2023).
- [5] “Optical CO2 Sensor Products.” Accessed: Jun. 19, 2023. [Online]. Available: <https://www.presens.de/products/co2>
- [6] J. Elhadj, M. Al-Hindi, and F. Azizi, “A Review of the Absorption and Desorption Processes of Carbon Dioxide in Water Systems,” *Ind. Eng. Chem. Res.*, vol. 53, no. 1, pp. 2–22, Jan. 2014, doi: 10.1021/ie403245p.
- [7] M. Al-Hindi and F. Azizi, “Absorption and desorption of carbon dioxide in several water types,” *Can. J. Chem. Eng.*, vol. 96, no. 1, pp. 274–284, Jan. 2018, doi: 10.1002/cjce.22901.
- [8] R. Sander, “Compilation of Henry’s law constants (version 4.0) for water as solvent,” *Atmos. Chem. Phys.*, vol. 15, no. 8, pp. 4399–4981, Apr. 2015, doi: 10.5194/acp-15-4399-2015.
- [9] A. G. Dickson and J. P. Riley, “The estimation of acid dissociation constants in seawater media from potentiometric titrations with strong base. I The ionic product of water K_w ,” *Marine Chemistry*, vol. 7, no. 2, pp. 89–99, 1979, doi: 10.1016/0304-4203(79)90001-X.
- [10] H. S. Harned and R. Davis, “The Ionization Constant of Carbonic Acid in Water and the Solubility of Carbon Dioxide in Water and Aqueous Salt Solutions from 0 to 50°,” *J. Am. Chem. Soc.*, vol. 65, no. 10, pp. 2030–2037, Oct. 1943, doi: 10.1021/ja01250a059.
- [11] H. S. Harned and S. R. Scholes, “The Ionization Constant of HCO_3^- - from 0 to 50°,” *J. Am. Chem. Soc.*, vol. 63, no. 6, pp. 1706–1709, Jun. 1941, doi: 10.1021/ja01851a058.
- [12] M. Dalal, *A text book of physical chemistry*, Dalal Institute, vol. 1. 2018.
- [13] X. Bobbia *et al.*, “Concordance and limits between transcutaneous and arterial carbon dioxide pressure in emergency department patients with acute respiratory failure: a single-center prospective observational study,” *Scand J Trauma Resusc Emerg Med*, vol. 23, no. 1, p. 40, Dec. 2015, doi: 10.1186/s13049-015-0120-4.
- [14] X. Ge *et al.*, “Development and characterization of a point-of-care rate-based transcutaneous respiratory status monitor,” *Medical Engineering & Physics*, vol. 56, pp. 36–41, Jun. 2018, doi: 10.1016/j.medengphy.2018.03.009.
- [15] T. N. Hansen, Y. Sonoda, and M. B. McIlroy, “Transfer of oxygen, nitrogen, and carbon dioxide through normal adult human skin,” *Journal of Applied Physiology*, Sep. 1980, doi: 10.1152/jappl.1980.49.3.438.
- [16] M.-P. Comsa, “Numerical methods for a personalized autonomous transcutaneous gas monitoring device,” Université Grenoble-Alpes, EEATS - Signal Image Parole Telecoms, 2022.

Skin Lesion Segmentation and Classification Using Deep Learning Methods

Spyridon Vollas
Hellenic Open University
Patras, Greece
std146179@ac.eap.gr

Isidoros Perikos
Compute Engineering & Informatics
Department
University of Patras
and Hellenic Open University
and Computer Technology Institute
and Press Diophantus
Patras, Greece
perikos@ceid.upatras.gr

Michael Paraskevas
Department of Electrical & Computer
Engineering Engineering
University of Peloponnese
and Computer Technology Institute &
Press Diophantus
Patras, Greece
mparask@cti.gr

Abstract— Melanoma is the most dangerous type of skin cancer. Every year hundreds of thousands of people are affected by this form of cancer, with tens of thousands of them leading to death. The diagnosis at an early stage is crucial and can lead to a complete cure of patients making it the most important parameter in the fight against it. The aim of this paper is to design and formulate deep learning methods and an ensemble schema for the accurate recognition of melanoma as well as of other skin lesions. The methods and the deep learning architectures that were designed and tested are convolutional neural networks, deep convolutional neural networks, deep residual networks as well as capsule networks. An ensemble method which consists of the DesNet121 and ResNet50 architectures is also designed and introduced. For the DenseNet121 and ResNet50 methods, the transfer learning technique was used for the phase of training. The experimental study revealed quite interesting results on the HAM10000 and ISIC 2019 datasets. The best performance among the methods was achieved by the DenseNet121 network with an accuracy up to 81%.

Keywords- melanoma; deep learning; ensemble learning; convolutional neural networks; capsule networks.

I. INTRODUCTION

Skin is the larger organ of the human body. Its main contributions are both avoiding infections and injuries and regulating body temperature. As with other organs of the body, the skin can be affected by cancer. Indeed, there are several types of skin cancer. The four main types are the Basal cell carcinoma, Squamous cell carcinoma, Merkel cell cancer and Melanoma [22].

Melanoma is the most dangerous type of skin cancer, and it is developed by melanocytes. These cells are responsible for the production of the natural skin pigment, melanin. It can metastasize to lymph nodes and internal organs of the human body. Untimely diagnosis leads in most cases to the death of patients. It can be developed in various parts of the human body and can progress in various ways. The main reasons that can lead to the appearance of melanoma are the exposure to ultraviolet (UV) radiation, especially from people with low levels of melanin (light skin), the possession of a large number of moles (>50), the presence of dysplastic nevus as well as some family (first-degree relatives) or personal history of melanoma or other types of skin cancer.

According to the Global Cancer Observatory (GCO) in 2020 324,635 new cases of melanoma were recorded worldwide (54% men and 46% women). There were also 57,043 new deaths with 57% of these being male. The continent most affected by skin cancer is that of North America at 32.4% of new cases.

As with all types of cancer, early diagnosis is crucial for the treatment of patients suffering from melanoma. For this purpose, several clinical methods have been developed for dermatologists to be able to identify and then proceed with the appropriate treatment of the disease [13][20]. Perhaps the most widespread technique is the ABCD mnemonic rule [3]. According to research studies, the characteristics of early-staged melanoma are similar regardless of the area in which they are located. These features can be easily remembered by thinking about the ABCD where, A refers to the asymmetry of the lesion, B refers to the fuzzy boundaries of the lesion, C refers to the uneven color of the lesion, D refers to the diameter of the lesion when it exceeds 6 mm.

The accurate diagnosis of skin cancer is considered to be a very challenging task, even for the most experienced dermatologists. Indeed, dermatologists with more than 10 years' of experience can achieve diagnostic accuracy of around 80% with the usage of clinical methods [10]. This is even lower for dermatologists with less experience. Thus, the development of an intelligent system with high accuracy in the classification of skin lesions is necessary for early diagnosis in a short time [16][18].

However, the automatic analysis of skin lesions is a very difficult and quite tricky task [8][11]. There are several reasons for that. First, there are cases where it is not easy to differentiate between benign and malignant skin lesions. Also, in most cases, the small diameter of the lesions does not allow to take high-resolution photographs with conventional cameras. Another reason that can lead to poor results is the slight contrast in the colors of the lesion and the patient's skin. This can make the boundaries of the lesion indistinguishable [2]. Finally, the presence of noises and artifacts inside a digital image can affect the task of classification. In general, noise is the result of errors in the image capture process that result in pixel values that do not reflect the actual intensities of the actual scene [17].

The purpose of this study is to design and develop deep neural networks and assess their performance in skin cancer

recognition. To that end, we formulate various deep learning methods and more specifically Convolutional Neural Networks (CNN), DenseNet121, ResNet50 and a capsule network. The designed methods were trained on various datasets and after that, an ensemble method that consists of DenseNet121 and ResNet50 networks was designed and developed.

II. RELATED WORK

Through the years, many studies have been conducted regarding the diagnosis and classification of skin cancer [5][19] and many works focus on the efficiency of convolutional neural networks in skin cancer recognition [1][12]. Authors in [14] proposed a method that consists of three stages. Firstly, for image preprocessing, the morphological closure function is applied to remove unwanted information from the images. Then the images were resized to have a size of 227x227 pixels. The faster-RCNN architecture was used to extract the features. This technique can detect and classify lesions of different types using the fully convolutional Region Proposal Network (RPN) and Fast-RCNN modules. The experiments showed that this method is robust to different image artifacts. Also, its performance can outperform existing techniques.

Zhang [21] used the EfficientNet network as the backbone of his architecture. More specifically, this network was used to extract features from the images contained in the dataset. For this purpose, transfer learning was used, where the weights of the pre-trained EfficientNet on the ImageNet dataset were used. The dataset used in this study was ISIC 2020 Challenge Dataset which was divided into a ratio of 7:2:1 for training, validation, and testing purposes respectively. The performance achieved by the proposed architecture is an AUK-ROC Score of 0.917 outperforming VGG16 and VGG19 networks.

In the work presented in [7], authors trained and tested eleven CNN architectures. Then the best-performing method was selected so that a mobile application could be created. The goal of this application will be to obtain images of skin lesions and be able to classify them into benign and malignant cases. The best performance of the networks tested was achieved by DenseNet169 which was the one chosen for the development of the Android application.

The authors in [6] proposed an architecture that is inspired by several advanced frameworks that are designed for the identification of skin lesions. This architecture which was named Lesion Classification Network (LCNet), consists of 11 blocks, and was trained end-to-end on dermoscopic skin cancer images. The experimental results showed that LCNet works better on large and balanced datasets and is reliable in predicting the correct lesion category.

The authors in [9] developed a two-stage model which will be responsible for melanoma detection. The first stage aims to accurately segment skin lesions images by using the U-Net architecture which was built on top of a Fully Convolutional Network (FCN). The second stage aims to predict the presence of melanoma using a deep residual network. The categorization results showed that the Dilated

Residual Network (DRN) should be fine-tuned for achieving better performance.

The aim of the study conducted by Ningrun et al. [15] was to create a melanoma detection model that can operate on devices with low computational power. For this purpose, they developed a framework that includes two architectures, one CNN and one that is a combination of CNN and an Artificial Neural Network (ANN). The experimental results showed the superiority of the CNN + ANN model in both performance and resistance to overfitting.

III. METHODOLOGY

In this section, we present the methodology of our work. The designed deep learning methods and the ensemble deep learning schema are illustrated and the exact way that they were trained is presented. Also, the dataset are presented too.

A. Datasets

As stated in Section I, the HAM10000 and ISIC 2019 datasets were used for both training and evaluation of the CNN architectures. These are two publicly available datasets containing RGB images in JPG format. HAM10000 is known as the Human Against Machine dataset and contains 10015 color images of skin lesions all 600x450 pixel size which were collected from dermatoscopic images from different populations. The ISIC 2019 contains a total of 33569 images of various sizes and the corresponding metadata, with entries such as age, sex, and general anatomic site. Here only the images belonging to the training set were used with their number being equal to 25331. These images are distributed to different classes depending on the type of skin lesion. The number of classes in HAM10000 is seven while ISIC 2019 has eight. The seven classes of HAM10000 are the Actinic keratoses (akiec), the Basal cell carcinoma (bcc), the Benign keratosis-like lesions (bkl), the Dermatofibroma (df), the Melanoma (mel), the Melanocytic nevi (nv) and the Vascular lesions (vasc). As HAM10000 is one of the datasets that constitutes the ISIC 2019 dataset, the latter contains the same classes as the former, with the one additional class being Squamous cell carcinoma (SCC).

For image preprocessing at first, we resize them for training more efficiently the CNN models. More specifically, the HAM10000 images were transformed from 600x450 pixels to 200x150 pixels, while the images of ISIC 2019 were transformed to have a size of 227x227 pixels. The images of both datasets were then normalized so that the values of each pixel were in the range [0, 1].

A very important technique that helps to train deep CNNs more efficiently, is that of data augmentation. Its use is considered particularly useful when the number of data is not sufficient for training deep architectures, as well as in cases where the distribution of data is uneven across the different classes of the dataset. Here, various augmentation techniques were used, such as random rotations at different angles, random zoom, random shear, vertical flips, as well as changes in the brightness of the images. Also, we random deleted 50% of the images belonging to class nv which was the dominant class of HAM1000.

For the augmentation of ISIC 2019 dataset, the ImageDataGenerator class of Keras was used. It can perform various image transformations in real time while the neural network is still in the training phase. One of the advantages of using this class is the fact that the architecture will receive new image transformations at each epoch, to reduce the possibility of overfitting. It also uses a small amount of RAM. The augmented datasets were split in a 70:20:10 ratio for training, evaluation, and testing purposes respectively. Finally, it is worth mentioning that the data is fed in the architectures in random order at each iteration during the phase of training.

B. Designed Deep CNN architectures

The main objective of this study is to design, examine and compare the performance of different CNN architectures. The methods that were used, are mainly CNN and Deep CNN techniques, an ensemble technique as well as a capsule network.

Firstly, for the experiments, a simple CNN architecture was used. It consists of 6 convolutional blocks with the first one containing one convolutional layer, one max pooling layer and one batch normalization layer. Blocks 2 and 3 are consisted of a convolutional and a max-pooling layer each, while blocks 4 and 5 contained a convolutional, a max-pooling and a dropout layer each. Finally, the last convolutional block has the same structure as blocks 2 and 3. On top of these, there are one flatten and 2 fully connected layers, the latter of which is responsible for the task of classification. The HAM10000 dataset was used for training the model. A visualization of the described method can be seen in the image below:

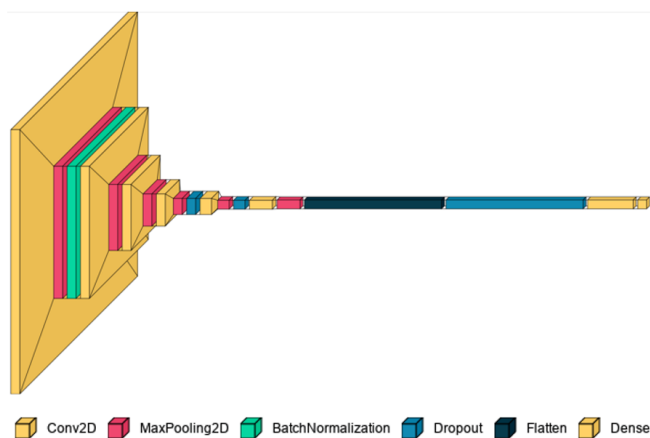


Figure 1. CNN model visualization

The first deep CNN network used for the experiments was the DenseNet121 network. The main advantage of this architecture is the resolution of the vanishing gradient descent problem. This problem occurs during backpropagation, and it can be more severe as new layers are added to a neural network. To address this problem, the researchers modified the connectivity pattern between layers. The standard CNN architecture connects each layer directly with the next one, while in DenseNet each layer is connected

directly with every layer that exists after it. This is accomplished by the dense blocks, one of the constituent elements of DenseNet. Inside a dense block, the size of the feature maps remains the same but the number of filters in each of them are different. Also, between them, layers that reduce the number of existing channels to half are placed. Those layers are called transition layers. Another benefit of DenseNet is the need of fewer parameters during training, making the network easier to train. DenseNet121 contains 121 layers, and the exact characteristics of it are illustrated in Table I.

TABLE I. STRUCTURE OF DENSENET121

Layers	Output size	DenseNet121
Convolution	112x112	7x7 conv, stride 2
Pooling	56x56	3x3 max pool, stride 2
Dense Block (1)	56x56	$\begin{bmatrix} 1 \times 1 \text{ conv} \\ 3 \times 3 \text{ conv} \end{bmatrix} \times 6$
Transition Layer (1)	56x56 28x28	1x1 conv 2x2 average pool, stride 2
Dense Block (2)	28x28	$\begin{bmatrix} 1 \times 1 \text{ conv} \\ 3 \times 3 \text{ conv} \end{bmatrix} \times 12$
Transition Layer (2)	28x28 14x14	1x1 conv 2x2 average pool, stride 2
Dense Block (3)	14x14	$\begin{bmatrix} 1 \times 1 \text{ conv} \\ 3 \times 3 \text{ conv} \end{bmatrix} \times 24$
Transition Layer (3)	14x14 7x7	1x1 conv 2x2 average pool, stride 2
Dense Block (4)	7x7	$\begin{bmatrix} 1 \times 1 \text{ conv} \\ 3 \times 3 \text{ conv} \end{bmatrix} \times 16$
Classification Layer	1x1	7x7 average global pool 1000D fully connected, softmax

From the structure above, the last layer which is responsible for classifying the data into the 1000 classes of ImageNet dataset was removed. After that, a dropout layer was added to deal with the problem of overfitting. A dropout layer randomly ignores the outputs of certain neurons of the previous layer. So, these outputs are not considered during backpropagation or forward propagation. Generally, overfitting occurs when the model has high variance. That means that the network performs well on the training dataset while on the evaluation dataset, its performance is degraded. In other words, the model learns to memorize the patterns existing in the training set. However, it does not have the ability to generalize for new data. Reasons such as the large number of hidden layers, usage of small datasets and data that contains noise can lead to overfitting. Finally, two dense layers were added with the last one having as a task the categorization of images into the classes ISIC 2019.

Next, we experimented with the ResNet50 architecture. It belongs to the family of Deep Residual Networks (DRNs) [4]. DRNs make use of residual blocks to overcome the problems associated with training deeper convolutional neural networks. In a network with residual blocks, a technique called skip connections is used. According to this,

training from a few layers can be bypassed if one of them harms the performance of the architecture. Thus, adding new layers will not affect the performance of the model, as normalization will override them if they are not useful. The ResNet50 is a fifty-layer deep architecture and a summary of the layers of which it is composed can be found in Table II.

TABLE II. STRUCTURE OF RESNET50

Layers	Output size	DenseNet121
conv1	112x112	7x7, 64, stride 2
conv2_x	56x56	3x3 max pool, stride $\begin{bmatrix} 1 \times 1, & 64 \\ 3 \times 3, & 64 \\ 1 \times 1, & 256 \end{bmatrix} \times 3$
conv3_x	28x28	$\begin{bmatrix} 1 \times 1, & 128 \\ 3 \times 3, & 128 \\ 1 \times 1, & 512 \end{bmatrix} \times 4$
conv4_x	14x14	$\begin{bmatrix} 1 \times 1, & 256 \\ 3 \times 3, & 256 \\ 1 \times 1, & 1024 \end{bmatrix} \times 6$
conv5_x	7x7	$\begin{bmatrix} 1 \times 1, & 512 \\ 3 \times 3, & 512 \\ 1 \times 1, & 2048 \end{bmatrix} \times 3$
Classification layer	1x1	average pool, 1000-d fc, softmax

As with DenseNet121, the last layer was removed. In its place were added two dropout and two dense layers. The first of the dense layers contains 256 nodes while the second one 8, one for every class of ISIC 2019.

C. Designed Ensemble Deep learning architectures

Ensemble learning is a deep learning approach in which the predictions of two or more methods are combined in order to achieve better results during categorization. There are different ensemble learning techniques. Here the weighted average was selected where different weights were assigned to each technique. More specifically, each model is multiplied by a weight, which value ranges between 0 and 1 and then their average is calculated.

For achieving better results during training of DenseNet121 and ResNet50 transfer learning was used. According to this technique an architecture that has been pre-trained on a larger dataset, can be used in a similar categorization task where the dataset is not so large. This leads to greater classification results. Here the pre-trained weights of ImageNet were used.

In addition to convolutional neural networks, we attempt to experiment with a special type of neural networks, which are the capsule networks. The main structural elements of these architectures are called capsules. A capsule consists of several neurons, each of which stores different information about the object it is trying to identify, into a multidimensional vector. Such information may be the position, the rotation, the scale of the object. Each capsule encodes the probability of an object being present in the image. One of the great advantages they offer is the elimination of the problem that can arise from the pooling operation. The purpose of this operation is to reduce the size

of the feature maps produced by convolutional layers. This is done to achieve the spatial invariance or in simpler words, regardless of the position of an object in the image, the method will be able to detect it and categorize it in the correct class. When reducing the dimension of the feature maps, useful information related to the rotation, position, scale, and various positional features of the object may be lost. Thus, the object detection and segmentation process becomes a quite challenging task. Finally, other advantages that capsule networks provide are that they need less amount of data during the phase of training, and their ability to better model hierarchical relationships.

The Capsule Network (CapsNet) designed and developed in our study, consists of an encoder and a decoder, each with a set of three layers. The encoder consists of a convolutional layer, a PrimaryCaps layer and a SkinCaps layer. On the other hand, the decoder consists of 2 fully connected layers. More specifically, the encoder consists of a convolutional layer which contains 256 filters of size 9x9, and ReLu is used as the activation function. Next, we have the PrimaryCaps layer. This is a convolutional layer which has 32 channels of eight-dimensional convolutional capsules (each capsule has 8 convolutional units with filters of size 9x9). Finally, the SkinCaps layer has 16 capsules per class, where each capsule receives input from the low-level capsule. A reconstruction loss is used to encode the initialization parameters. The decoder receives the correct 16-dimensional capsule and decodes it into an image. None of the incorrect capsules are considered. The loss is calculated by finding the Euclidean distance between the input image and the reconstructed one.

The experiments were conducted using Tensorflow and Keras libraries. More specifically, for the training and evaluation of CNN, DenseNet121 and ResNet50 methods Tensorflow version 2.8.2 and Keras version 2.8.0 were used. The goal was to find those that would give the best possible performance. The parameters used for tuning the networks are seen in Table III.

TABLE III. MODEL TRAINING PARAMETERS

Model Parameter	CNN	DenseNet121	ResNet50	CapsNet
Optimizer	Adam (lr=3e-4)	Adam (lr=5e-5)	Adam (lr=3e-5)	Adam (lr=0.001)
Loss Function	Categorical crossentropy	Categorical crossentropy	Categorical crossentropy	Mean Absolute Error
Batch Size	16	32	32	32
Epochs	100	30	30	25

An optimizer is an algorithm used to increase the efficiency of the neural network. It depends by the learning parameters of the neural network, the weights, and biases, and help us to know how these parameters should be changed in order to reduce the losses during categorization. Categorical cross-entropy loss function measures the

performance of a classification model whose output is a probability value between 0 and 1. This value is being increased as the predicted probability deviates from the actual class. It is used in cases where the data is categorized into more than two classes. As for the Mean Absolute Error, this function calculates the absolute difference between the current output and the expected output divided by the number of outputs. Its objective is to minimize these absolute differences. Finally, batch size is a hyperparameter that determines the number of data instances that the network must process before it updates its internal parameters.

IV. EXPERIMENTAL STUDY

A concrete experiment was designed and conducted with the aim to assess the performance of the deep learning methods and the ensemble schema. Publicly available datasets were utilized and different types of data were used to assess the performance of the methods, and also provide a deeper insight into their performance on heterogeneous data from different sources. The experiments were conducted in the virtual environment of Google Colab. This is a Google Research product which allows anyone to write and execute Python code via a hosted Jupyter notebook service. To measure the performance of the designed methods accuracy, precision, recall and F1-score were used and were calculated. The main results are presented in Table IV.

TABLE IV. PERFORMANCE OF TESTED MODELS DURING THE TRAINING PHASE

Model	Accuracy	Precision	Recall	F1-Score
CNN	81.05%	85.14%	75.54%	80.06%
DenseNet121	81%	85.09%	77.73%	81.24%
ResNet50	79.5%	84.53%	75.25%	79.64%
Ensemble Method	80.85%	-	-	-
CapsNet	66.89%	-	-	-

As illustrated in Table IV, the best performance among all the designed and developed models, was achieved by the DenseNet121 network. It can be also observed that the architecture that was most prone to overfitting was the ResNet50 network. So, that was the main reason why two dropout layers were added to the network just after the main pre-trained method (as opposed to DenseNet121 network in which only one dropout layer was desired to be added). In the figures below, we present the loss and the accuracy diagrams of all the designed methods.

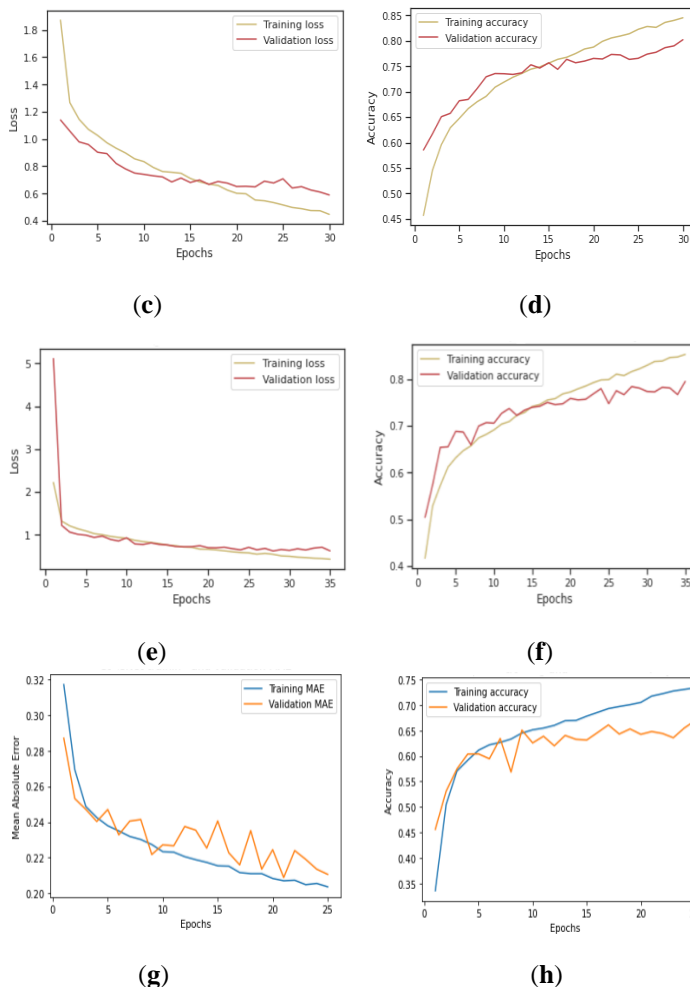
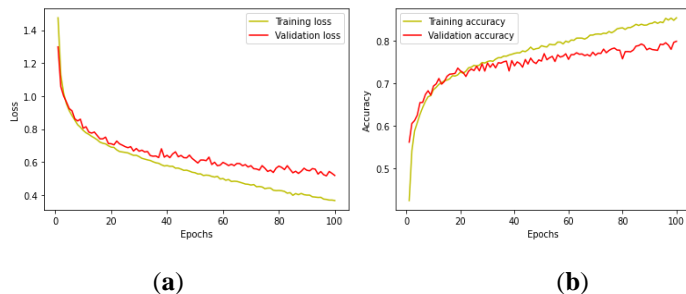


Figure 2. Accuracy and loss of tested methods during training: (a), (b) Loss and accuracy diagrams of CNN method; (c), (d) Loss and accuracy diagrams of DenseNet121; (e), (f) Loss and accuracy diagrams of ResNet50; (g), (h) Loss and accuracy diagrams of CapsNet.

The lowest performance of the architectures is that of the capsule network. As mentioned in the previous section these architectures have several advantages over traditional CNNs. However, in our study, they only achieved very good performance on simple datasets without having a correspondingly good performance on more complex ones.

V. CONCLUSIONS

In the context of our work, various deep learning architectures as well as an ensemble deep-learning schema was designed and formulated. The datasets used were HAM10000 and ISIC 2019. The best performance was achieved by the method Dense-Net121 with an accuracy of 81% and F1-Score = 81.24%. The ensemble method which consisted of the DenseNet 121 and ResNet50 networks, achieved slightly lower results when the weighted averaging technique was used for calculating its performance.

There are many directions that future work could examine. First, experiments with additional dermoscopic datasets can be conducted. Such datasets can be the ISIC

2020 which contains 33126 images of skin lesions which is significantly bigger than the datasets used in this study. Another step that we can take into consideration is the study and experimentation with more sophisticated ensemble learning techniques in order to achieve better results during the classification. For example, stacking multiple machine learning models is an advanced ensemble learning technique in which different models are trained and their combined outputs are used as inputs to another machine learning algorithm called a meta-learner.

REFERENCES

- [1] A. Adegun and S. Viriri, "Deep learning techniques for skin lesion analysis and melanoma cancer detection: a survey of state-of-the-art," *Artificial Intelligence Review*, 2021, 54(2), pp. 811-841.
- [2] A. Dutta, M. K. Hasan, and M. Ahmad, "Skin Lesion Classification Using Convolutional Neural Network for Melanoma Recognition," *bioRxiv*, 2020. <https://doi.org/10.1101/2020.11.24.20238246>.
- [3] R. J. Friedman, D. S. Rigel, and A. W. Kopf, "Early Detection of Malignant Melanoma: The Role of Physician Examination and Self-Examination of the Skin," *CA Cancer J. Clin.* 1985, 35 (3), pp. 130–151.
- [4] K. He, X. Zhang, S. Ren, and J. Sun, "Deep Residual Learning for Image Recognition," In 2016 IEEE Conference on Computer Vision and Pattern Recognition, IEEE, 2016.
- [5] R. Javed, M. S. M. Rahim, T. Saba, and A. Rehman, "A comparative study of features selection for skin lesion detection from dermoscopic images," *Network Modeling Analysis in Health Informatics and Bioinformatics*, 2020.
- [6] R. Kaur, H. GholamHosseini, R. Sinha, and M. Lindén, "Melanoma Classification Using a Novel Deep Convolutional Neural Network with Dermoscopic Images," *Sensors (Basel)* 2022, 22 (3), pp. 1134. <https://doi.org/10.3390/s22031134>.
- [7] I. Kousis, I. Perikos, I. Hatzilygeroudis, and M. Virvou, "Deep Learning Methods for Accurate Skin Cancer Recognition and Mobile Application," *Electronics (Basel)* 2022, 11 (9), pp. 1294. <https://doi.org/10.3390/electronics11091294>.
- [8] S. Manzoor et al., "Melanoma Detection Using a Deep Learning Approach," *Vol 4 Issue 1 2022*, 4 (1), pp. 222–232. <https://doi.org/10.33411/ijist/2022040117>.
- [9] J. Millenia, M. F. Naufal, and J. Siswanto, "Melanoma Detection Using Convolutional Neural Network with Transfer Learning on Dermoscopic and Macroscopic Images," *J. inf. syst. eng. bus. intell.* 2022, 8 (2), pp. 149–161. <https://doi.org/10.20473/jisebi.8.2.149-161>.
- [10] C. A. Morton and R. M. Mackie, "Clinical Accuracy of the Diagnosis of Cutaneous Malignant Melanoma," *Br. J. Dermatol.* 1998, 138 (2), pp. 283–287. <https://doi.org/10.1046/j.1365-2133.1998.02075.x>.
- [11] I. Mporas, I. Perikos, and M. Paraskevas, "Color models for skin lesion classification from dermoscopic images". In *Advances in Integrations of Intelligent Methods: Post-workshop volume of the 8th International Workshop CIMA 2018*, Volos, Greece, November 2018 (in conjunction with IEEE ICTAI 2018) (pp. 85-98). Springer, 2020.
- [12] A. Naeem, M. S. Farooq, A. Khelifi, and A. Abid, "Malignant melanoma classification using deep learning: datasets, performance measurements, challenges and opportunities," *IEEE Access*, 2020, 8, pp. 110575-110597.
- [13] P. Naronglerdrit, I. Mporas, I. Perikos, and M. Paraskevas, "Pigmented skin lesions classification using convolutional neural networks". In *2019 International Conference on Biomedical Innovations and Applications (BIA)*, pp. 1-4, IEEE, 2019.
- [14] M. Nawaz et al., "Melanoma Localization and Classification through Faster Region-Based Convolutional Neural Network and SVM," *Multimed. Tools Appl.* 2021. <https://doi.org/10.1007/s11042-021-11120-7>.
- [15] D. N. A. Ningrum et al. "Deep Learning Classifier with Patient's Metadata of Dermoscopic Images in Malignant Melanoma Detection," *J. Multidiscip. Healthc.* 2021, 14, pp. 877–885.
- [16] S. Sonthalia S. Yumeen and F. Kaliyadan, "Dermoscopy Overview and Extradagnostic Applications," [Updated 2022 Aug 8]. In: *StatPearls [Internet]*. Treasure Island (FL): StatPearls Publishing; Jan. 2022, Available from: <https://www.ncbi.nlm.nih.gov/books/NBK537131>
- [17] K. Thurnhofer-Hemsi and E. Domínguez, "A Convolutional Neural Network Framework for Accurate Skin Cancer Detection," *Neural Process. Lett.* 2021, 53 (5), pp. 3073–3093, <https://doi.org/10.1007/s11063-020-10364-y>
- [18] S. Tiwari, "Dermatoscopy using multi-layer perceptron, convolution neural network, and Capsule network to differentiate malignant melanoma from benign nevus," *Int. J. Healthc. Inf. Syst. Inform.* 2021, 16 (3), pp. 58–73. <https://doi.org/10.4018/ijhisi.20210701.oa4>.
- [19] B. N. Vinay, P. J. Shah, V. Shekar, H. R. Vanamala and V. Krishna, "Detection of Melanoma Using Deep Learning Techniques," In *2020 International Conference on Computation, Automation and Knowledge Management (ICCAKM)*, IEEE, 2020.
- [20] H. Zanddizari, N. Nguyen, B. Zeinali, and J. M. Chang, "A New Preprocessing Approach to Improve the Performance of CNN-Based Skin Lesion Classification," *Med. Biol. Eng. Comput.* 2021, 59 (5), pp. 1123–1131. <https://doi.org/10.1007/s11517-021-02355-5>
- [21] R. Zhang, "Melanoma Detection Using Convolutional Neural Network," *2021 IEEE International Conference on Consumer Electronics and Computer Engineering (ICCECE)*, Guangzhou, China, 2021,, pp. 75-78, doi: 10.1109/ICCECE51280.2021.9342142
- [22] Cancer types, 2022, <https://www.cancer.net/cancer-types/skin-cancer-non-melanoma/introduction>